Fuel 378 (2024) 132901

Contents lists available at ScienceDirect

Fuel

journal homepage: www.elsevier.com/locate/fuel

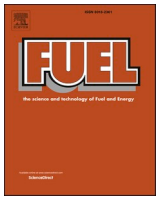

Full Length Article

Advanced visualisation of biomass charcoal combustion dynamics using MWIR hyperspectral and LWIR thermal imaging under varied airflow conditions

Yufeng Lai [a], Xuanqi Liu [b,c,*], Muyi Pan [d], Matthew Davies [a], Callum Fisk [a], David King [e], Yang Zhang [f], Jon Willmott [a,*]

[a] Department of Electronic and Electrical Engineering, The University of Sheffield, Sheffield, S1 4ET, United Kingdom
[b] School of Low-Carbon Energy and Power Engineering, China University of Mining and Technology, Xuzhou 221116, China
[c] Research Centre for Smart Energy, China University of Mining and Technology, Xuzhou 221116, China
[d] College of Intelligent Equipment, Suzhou Vocational Institute of Industrial Technology, Suzhou 215000, China
[e] Advanced Manufacturing Research Centre, the University of Sheffield, Rotherham, S60 5TZ, United Kingdom
[f] Department of Mechanical Engineering, The University of Sheffield, Sheffield S1 3JD, United Kingdom

ARTICLE INFO

Keywords:
Biomass charcoal combustion
Combustion efficiency
MWIR hyperspectral imaging
LWIR thermal imaging
Air supply
Gas emissions

ABSTRACT

Biomass charcoal combustion is a complex process, significantly influenced by various operating parameters. Among these parameters, air supply emerges as a critical factor affecting combustion efficiency, gas emissions, and thermal dynamics. In this study, we explored these complex interdependencies using a novel combination of mid-wavelength infrared (MWIR) hyperspectral imaging and long-wavelength infrared (LWIR) thermal imaging, under different airflow rates. Our findings demonstrated that while increased airflow accelerated the overall combustion rate, it simultaneously decreased combustion efficiency. Specifically, the thermal profiles showed an increased surface temperature at a low flowrate (0.5 L/min) while decreasing in temperature with higher flowrates. The decreased system temperature led to a lower combustion efficiency because of the reduced conversion rate from combustible gases (CH_4 and CO) into CO_2 and H_2O. Additionally, the results also demonstrated that cooling effects of the high flowrates primarily impeded the solid-phase combustion stage. This is further corroborated by the temporal and spatial variation in the emissions of key gas species (H_2O vapor, CH_4, CO, and CO_2) observed through hyperspectral imaging. The emission evolution of these gases displayed the different stages of the gas-phase and solid-phase combustion. The spatial distribution of the trace gases showed a decreased distribution radius due to the enhanced diffusion to the fuel surface when the airflow increases, aligning well with the two-film model established in the literature. Furthermore, we utilised spectral radiance ratios (CO/CO_2, CH_4/CO_2, H_2O/CO_2) to gain additional insights into the combustion dynamics. These ratios evidenced the decrease in combustion efficiency at high airflow rates. Finally, the increased H_2O/CO_2 ratio further demonstrated the impeded char combustion and a shift towards pyrolysis at higher airflow rates because of the decreased thermal equilibrium of the system. The findings from this study provide critical insights into the dynamics of biomass charcoal combustion and illuminates the path for optimising energy efficiency and assessing the environmental implications from burning biomass fuels.

1. Introduction

Combustion processes play a vital role in the world's energy systems, underlying applications from power generation to waste disposal [1]. Charcoal, derived from biomass, offers high calorific value and low ash content, making it ideal for energy production across various settings, from industrial to domestic uses in developing areas [2].

Despite its benefits, biomass combustion also poses environmental challenges, notably in the form of pollutant gas emissions such as CH_4, CO and NOx. Understanding and controlling the variables that influence

* Corresponding authors at: School of Low-Carbon Energy and Power Engineering, China University of Mining and Technology, Xuzhou 221116, China (X. Liu). Department of Electronic and Electrical Engineering, The University of Sheffield, Sheffield, S1 4ET, United Kingdom (J. Willmott).
E-mail addresses: xuanqi.liu@cumt.edu.cn (X. Liu), j.r.willmott@sheffield.ac.uk (J. Willmott).

https://doi.org/10.1016/j.fuel.2024.132901
Received 10 April 2024; Received in revised form 20 August 2024; Accepted 22 August 2024
Available online 26 August 2024

these emissions is critical for mitigating potential environmental risks and improving combustion efficiency [3].

A critical factor in the combustion process is the airflow supply [4]. Its role extends beyond merely enhancing oxygen availability or exerting cooling effects, as traditionally perceived [2]. Airflow crucially influences combustion dynamics, efficiency, and the equilibrium between pyrolysis and combustion phases. However, the current understanding of how specific airflow rates impact biomass combustion remains incomplete. This gap in knowledge partly arises from the limitations of traditional diagnostic tools which struggle to capture the gas field in biomass combustion processes effectively.

Existing gas detection techniques such as Particle Image Velocimetry (PIV) provide valuable insights into the velocity fields of fluid flow but do not offer chemical specificity. Laser-based detection methods like Planar Laser-Induced Fluorescence (PLIF) predominantly utilise UV to NIR wavelengths and are thus generally limited to detecting fluorescent species, primarily radicals, and typically do not cover MWIR wavelengths where the gas species have strong emission. Additionally, the laser-based technology requires complex alignment and a controlled working environment, making it difficult to use in biofuel combustion systems. Traditional gas probing techniques can directly measure concentration but lack spatial resolution, which is crucial for understanding complex dynamic processes. Other visualisation methods, such as those employing narrow-band filters, are constrained by the spectral resolution allowed by the filter bandwidth and cannot simultaneously measure multiple species.

Research on charcoal, coal combustion and their emissions are integral to energy and environmental science, aiming to improve energy efficiency and achieve a better emission control [2]. For example, the emission rate (ER) of CO/CO_2 has been considered as an indicator of the combustion efficiency [5]. Traditional analysis methods, including flue gas analysis, thermogravimetric analysis and mass spectrometry, have highlighted how those factors such as fuel properties, system temperature, and airflow supply rate significantly influence combustion efficiency and gas emissions [6,7]. However, these methods often fail to provide the spatial and temporal detail necessary for an intricate understanding of combustion dynamics and the environmental impact. For example, emissions from combustion processes, particularly CO and CH_4, pose environmental challenges due to their potent greenhouse effects [8]. And their intensity and spatial distributions can be highly depending on the combustion stages combustion stages [9]. Consequently, there is a pressing need for novel methodologies that can offer detailed and dynamic characterisation of biomass combustion processes and monitor the emissions simultaneously.

Recent advances in imaging techniques present new opportunities to explore these impacts in detail [10,11]. This study employs a novel technique of Mid-Wavelength Infrared (MWIR) Hyperspectral Imaging (HSI) to map different gas-phase species produced during combustion. Despite its demonstrated utility in other fields, the adoption of MWIR HSI in combustion studies has been limited, marking an area of untapped potential [12,13]. To provide additional context to the hyperspectral data, Long-Wavelength Infrared (LWIR) thermal images were taken simultaneously, affording detailed thermal fields of the burning charcoal surface [14].

This work introduces novel implementation of MWIR HSI and LWIR thermal imaging to analyse charcoal combustion under varying airflow conditions. In doing so, it reveals new insights into the impacts of airflow rates on the spatial–temporal patterns of gas emissions, the balance between complete and incomplete combustion, the pyrolysis and combustion. The findings offer implications for optimising combustion processes, enhancing combustion efficiency, and mitigating environmental risks associated with biomass combustion, with potential broader implications for the field of energy production. The advanced diagnostic approaches proposed herein demonstrate promising results for enhancing observation capabilities within the next-generation energy industry.

2. Methodologies

2.1. Experimental arrangement

The experimental setup is illustrated in Fig. 1(a). Charcoal cubes made from coconut shells were selected as the test samples in the work because they are common in domestic and industrial applications. In addition, the combustion of charcoal consists of both solid-phase combustion (primary) and gas-phase flaming [15], which is representative of biomass fuels. The dimension of the cube-shaped samples is 25 mm × 25 mm x 25 mm with the error under ±1 mm. The initial weight was measured as an averaged 63.5229 g with a standard deviation of 0.1009 g.

A premixed methane-air burner with a nozzle 9.6 mm in diameter was used to ignite the samples with air and methane flowrates of 1 L/min and 4 L/min respectively. A mesh holder was designed for the purpose of minimising the interference of the flow field. Each sample was pilot ignited for 20 s, then the methane supply was cut off and the demand flowrate of compressed air was applied.

This work used 5 different airflow supply: 0 L/min (as control), 0.5 L/min, 1.5 L/min, 3.0 L/min and 4.5 L/min, to investigate the charcoal combustion changes under different airflow supply conditions. The airflow rates were determined after pre-tests with consideration to cover a range from minimal to significant influence on the combustion dynamics. The work pressure can be considered as the ambient atmospheric pressure of the open environment experiments. In practical applications, such as grilling or traditional cooking stoves, it is common to allow airflow from underneath for promoting more efficient combustion [5,16]. Given the primary role of airflow supply in altering air/oxygen availability and its relevance to practical scenarios in domestic and industrial settings, precise control over the flow field is not essential for the purposes of this study.

The charcoal sample was placed on a designed mesh holder to minimise the impact on the surrounding flow field [17]. The sample along with the holder were placed on an analytical balance (ADAM NBL 84i) with a precision of 0.1 mg. The lifting effect of upward airflow on weight was pre-calibrated and subtracted from the weight. The results were then normalised to their initial value to allow a comparison of the weight loss.

The combustion process of charcoal was recorded thermally by a long-wavelength infrared (LWIR) camera (PyrOptik, model LW640) and spectrally by a mid-wavelength hyperspectral imaging (MWIR HSI) camera (Specim, FX50, 16 bits, 640 pixels spatial resolution). The MWIR HSI camera employs a push-broom scan in order to record hyperspectral images. An image of scene was cropped by a slit (19.2 μm) and then dispersed across a MWIR focal plane array. The 3-D spectral-temporal data cube was acquired and can be subsequently reconstructed into a spatial-spectral image cube with the post-processing. The camera was fixed on a translation stage which allowed the camera to scan transversely to cover the full extent of the sample. Each scan took about 10 s and another 10 s for data storage and camera cooling, thus a time averaged HSI of 10 s with 10 s interval can be obtained. The total recording time was 30 min, starting when the airflow was applied. Each flowrate was repeated 5 times, to quantify repeatability. Considering the stable and consistent combustion process of charcoal (homogeneity), the deviation in the emission during the scanning process is assumed to be minimal.

2.2. Calibrations

The MWIR HSI camera was spectrally calibrated by the manufacturer in the range of 2707.9 nm to 5278.6 nm in 308 channels. The nonuniform spectral response along the wavelength was determined in the lab by comparison to Planck's Law of an ideal blackbody. The spectral radiance of a blackbody at a given temperature, is given as Eq. (1):

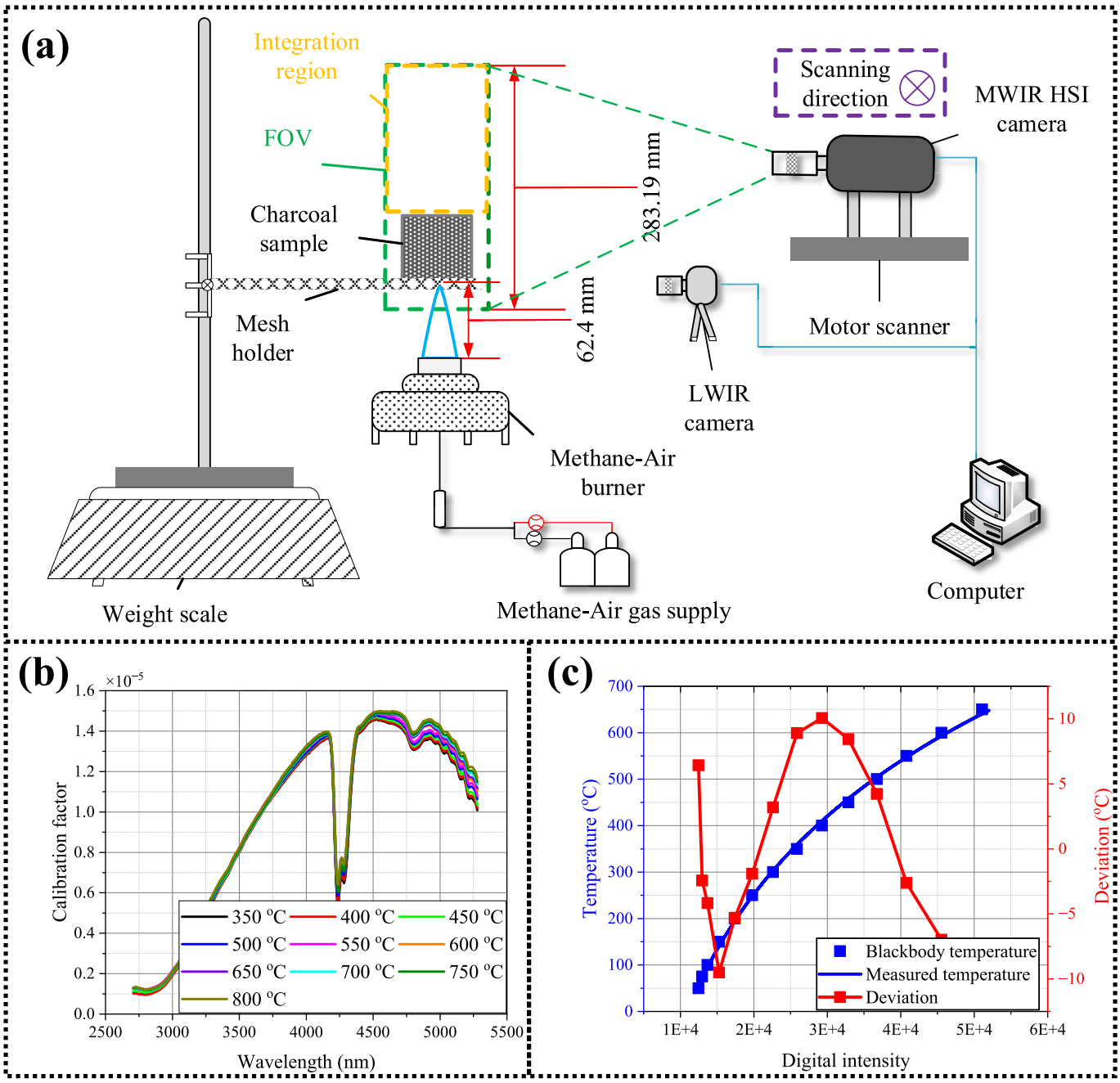

Fig. 1. Experimental arrangement and pre-calibrations: (a) experiment setup; (b) calibration factor of MWIR HSI system and (c) radiance calibration and uncertainty of LWIR thermal camera.

$$B(\lambda, T) = \frac{(2hc^2)}{\lambda^5} * \frac{1}{e^{hc/\lambda kT} - 1} \quad (1)$$

where B(λ, T) is the blackbody radiation, h is Planck's constant, c is the speed of light, λ is the wavelength, k is Boltzmann's constant, and T is the absolute temperature.

The camera was scanned transversely and captured images of a blackbody furnace (emissivity ~0.99) temperature ranging from 350 °C to 800 °C with 50 °C increment. The digital level ($DL(\lambda, T)$) along with the wavelength at different temperature can be obtained after subtracting the dark offset value from the digital-logic-levels spectrally. The calibration factor F can be obtained by calculating the ratios between the spectral radiance and the digital level [18], as shown in Eq. (2):

$$F(\lambda, T) = \frac{DL(\lambda, T)}{B(\lambda, T)} \quad (2)$$

Fig. 1(b) shows the results of the calculated $F(\lambda, T)$. It is found the ratios were relatively consistent with different blackbody temperatures, which means $F(\lambda, T)$ is less dependent on the temperature. The actual spectral radiance could then be calculated by dividing the averaged calibration factor $\overline{F}(\lambda)$ by the camera digital level $DL(\lambda)$ for each wavelength band, shown as Eq. (3):

$$I(\lambda, T) = DL(\lambda, T)/\overline{F}(\lambda). \quad (3)$$

The width-height ratio of the HSI was corrected by scanning a 25 mm aperture in the front of the blackbody furnace. The width-height ratio of the HSI was calculated as 40:1 which was used for reconstructing the

images.

The LWIR thermal camera was sensitive from 7.5 μm to 13.5 μm which enabled it to detect the whole temperature range during the charcoal combustion. The camera resolution was 640 × 512 pixels with a fixed framerate of 9 Hz. The calibration was based on Planck's Law [19] using a blackbody furnace (emissivity >0.99) from 50 °C to 650 °C. The uncertainty was determined as the deviation between the calculated temperature and the blackbody temperature, which was under 10 °C at all measured temperatures, shown as Fig. 1(c). The temperature of the side surface of the charcoal was averaged and compared with different airflow conditions.

2.3. HSI processing

The raw HSI data was in a 3-D spectral-temporal data cube. The dark frames were captured before each experiment and the offset from zero digital-logical-levels from the raw data cube can be removed. Then the spectral-temporal data cube was subsequently reconstructed into a spatial-spectral image cube. The calibration factors (Fig. 1(b)) were applied to the data cube to obtain the spectral radiance and eliminate the non-uniformity of the camera sensor.

Charcoal combustion is a complex process which consists of the thermal pyrolysis process (producing combustible species such as CH_4, CO, H_2, C_2H_6…), flaming combustion and solid-phase combustion [6]. Considering CH_4 is the dominate volatile organic compounds (VOCs) in the biomass pyrolysis process [3,20], the key species in charcoal combustion which emit radiance in the mid-wavelength are H_2O vapour, CH_4, CO, CO_2 and NO [16]. NO emission was not presented in this work considering its low concentration and irrelevance to the combustion efficiency. Fig. 1 (a) shows the region-of-interest (ROI) (Yellow dash-line) which covers the primary region of the gas-phase products, and the spectral radiance was integrated in the ROI to show a comparable emission of the charcoal combustion. Fig. 2(b) shows the typical spectrum of gases generated from charcoal combustion. The emission bands were identified by comparison to the HITRAN database [21]. The radiance at single wavelength was then integrated along the identified band of each gas species. This could quantify the spectral radiance of certain species in the mid-wavelength range.

The integrated spectral radiance that represents individual gas species was then normalised with a global maximum to restrict the values within 16-bit for display purposes. The final HSI which provides the direct visualisation of the gas distributions can be obtained after conducting the spatial correction (40:1) and applying the colour map.

2.4. Gas species emission

The absolute spectral radiance depends on many factors such as spectral emissivity and temperature, therefore the measured radiance intensity cannot directly reflect the level of each gas species concentration.

The spectral radiance of a specific gas species can be expressed as Eq. (4):

$$I(\lambda, T) = A^{*}n^{*}\int_{\lambda_1}^{\lambda_2} \varepsilon(\lambda, T)^{*}B(T, \lambda)d\lambda \tag{4}$$

where A represents the physical constants of the system such as geometric length and pressure of the gas, n is the concentration of the gas, $B(\lambda, T)$ is the blackbody radiation, $\varepsilon(\lambda, T)$ is the relative emissivity (or the emission coefficient) of gas. Assuming that the different gas species are in thermal equilibrium, have the same pressure at the same location and the same dilution level caused by the airflow supply, their spectral radiance ratio can be defined as Eq. (5):

$$I_A(\lambda_A, T)/I_B(\lambda_B, T) = \frac{n_A}{n_B}{}^{*}\frac{\varepsilon_A(\lambda_A, T)}{\varepsilon_B(\lambda_B, T)}{}^{*}\frac{B_A(\lambda_A, T)}{B_B(\lambda_B, T)} \tag{5}$$

In this equation, the term $\frac{\varepsilon_A(\lambda_A,T)}{\varepsilon_B(\lambda_B,T)}{}^{*}\frac{B_A(\lambda_A,T)}{B_B(\lambda_B,T)}$ remains constant for given λ_A, λ_B and temperature. Consequently, the spectral radiance ratio offers insight into the relative concentration ratio of the two species: $\frac{n_A}{n_B}$. In addition, the dilution effects of the varied airflow can be considered as negligible due to the same level of influence on different gas species. The ratio approach has been widely used in remote sensing [22,23] for concentration estimation. Similarly, the relative percentage of each gas species $\frac{n_A}{n_{total}}$ can be calculated.

The method provides a basic representation of the gas concentration, under the assumption regarding the consistency of the term $\frac{\varepsilon_A(\lambda_A,T)}{\varepsilon_B(\lambda_B,T)}{}^{*}\frac{B_A(\lambda_A,T)}{B_B(\lambda_B,T)}$. This assumption is justified by the fact that $\frac{n_A}{n_B}$ is predominantly affects Eq. (5) while the variations are negligible given the confined wavelength range and relatively insignificant temperature change in this study [24,25]. Nevertheless, the spectral intensity ratio can serve as an indicator for characterising the combustion process, presenting its temporal evolution and the effects of varied airflow supply.

3. Results and discussions

3.1 wt. loss and total combustion rate

The weight loss rate under different air flow supply were normalised and presented in Fig. 3. They exhibited a clear increase trend with the airflow increasing from control to 4.5 L/min. The increasing burning rate with higher airflow has been demonstrated in the literature [7]. This weight loss can be attributed to two primary processes: combustion and thermal pyrolysis [26]. Both of these processes contribute to the reduction of the mass of the original biomass charcoal. While

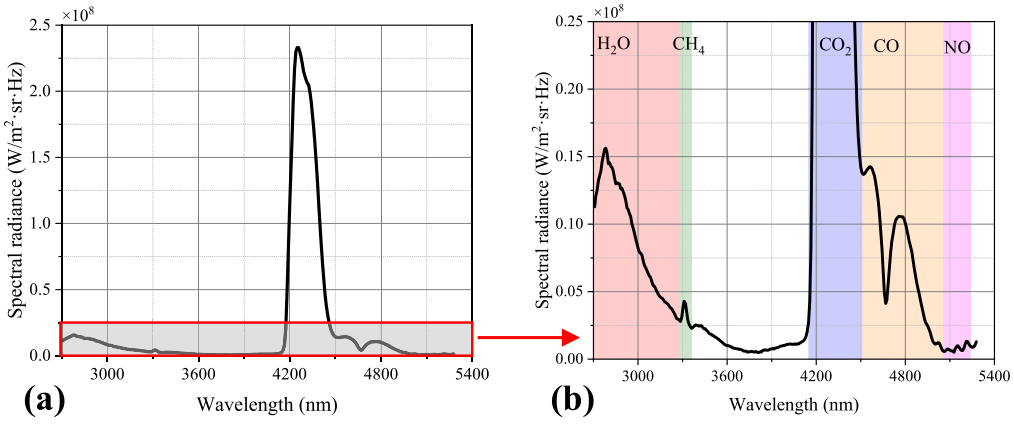

Fig. 2. (a) Example spectrum of charcoal gas products. (b) The identified species are based on HITRAN database [21].

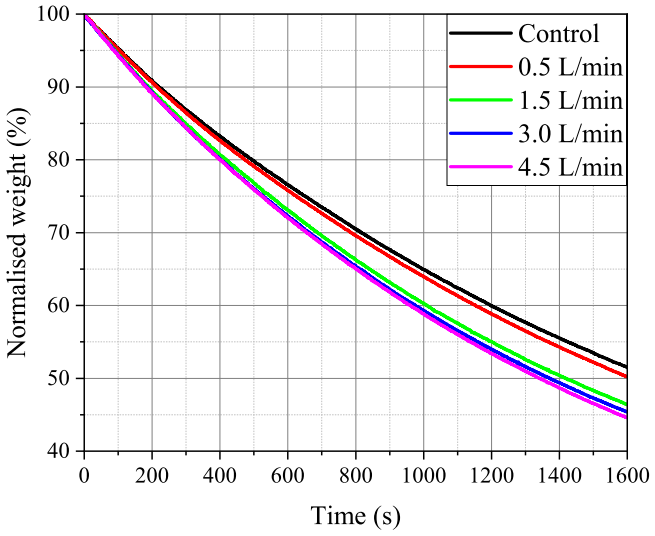

Fig. 3. Weight loss of the charcoal samples under different air flowrates.

combustion involves oxidation reactions with oxygen, thermal pyrolysis refers to thermal decomposition processes which may occur in both oxygen-rich and oxygen-deficient environments. Combustion predominantly results in products such as CO_2 and water, while thermal pyrolysis generates a variety of gaseous products including CO, CH_4, and other volatile species [26].

In the early stages of combustion, the biomass charcoal undergoes thermal pyrolysis primarily due to elevated temperatures, which leads to the release of volatile gases. As combustion proceeds, the availability of these volatiles and additional supply of oxygen influences the subsequent processes [27]. The higher in weight loss rate with the increase in airflow supply could be attributed to the greater supply of oxygen, promoting the global decomposition rate [27]. The oxygen facilitated the combustion reactions which contributed to the weight loss of the biomass charcoal. Concurrently, the increased flowrate aided the diffusion of the oxygen into the charcoal surface which enhanced the formation of both CO and CO_2 from the solid fuel surface [28]. Therefore, the enhanced weight loss at higher airflow rates indicates the effects on combustion and pyrolysis processes, both of which contribute to the overall weight loss rate.

The weight loss serves as an indicator of fuel consumption rate, but without revealing the underlying dynamics between the competitive processes of combustion and pyrolysis. The dominance of each process is intricately linked to oxygen availability and temperature conditions [29]. Interestingly, the introduction of airflow simultaneously enhances oxygen accessibility while potentially reducing system temperature. A thorough investigation of these complex dynamics, which requires a multifaceted approach, is discussed in subsequent sections.

3.2. Thermal characteristics of combustion

Fig. 4 shows the surface temperature distributions under different airflow rates at three time points (t = 50 s, t = 220 s and t = 600 s). It can be observed that the initial stages of the combustion (t = 50 s), the whole charcoal fuel underwent a uniform and relatively high temperature. The airflow did not significantly impact the surface temperature at this point. When the combustion proceeded to t = 220 s, there were more significant differences presented across the flow conditions. Under low airflow conditions (control and 0.5 L/min), the charcoal surface exhibited a relatively uniform temperature distribution, with cooling at both side edges, which was attributed to natural convection cooling in the absence of forced airflow. The surface temperature under 0.5 L/min appeared higher than the control. However, at higher flow rates (e.g., 4.5 L/min), the temperature distribution presented a distinct pattern with a noticeable cooling effect at the bottom. This was due to the forced convective cooling from the higher airflow impinging on the charcoal's surface. The impact of the different flow conditions also resulted in the later stage of the combustion (t = 600 s). It can be seen that the nonuniformity increased with the higher flowrates and the temperature was relatively low when a high airflow was applied.

Fig. 5 presents the quantitative perspective on the time-evolution of the average surface temperature. The profiles indicate that the surface temperature typically increased rapidly to reach an initial peak, then dropped to a lower point before gradually increasing again and eventually stabilising at a relatively consistent level.

This trend is consistent with the known stages of biomass combustion [24,27,30]. Initially, thermal pyrolysis led to the release and subsequent ignition of volatile gases, causing a swift temperature rise. The initial peak represented the phase of intense volatile combustion. The ensuing temperature drop indicated the depletion of volatiles and the onset of char combustion. The gradual increase and subsequent plateau of temperature signified the more stable, though slower, combustion of char.

It is found that the average surface temperature tended to decrease with the increased airflow rate. This indicated that a low flowrate (0.5

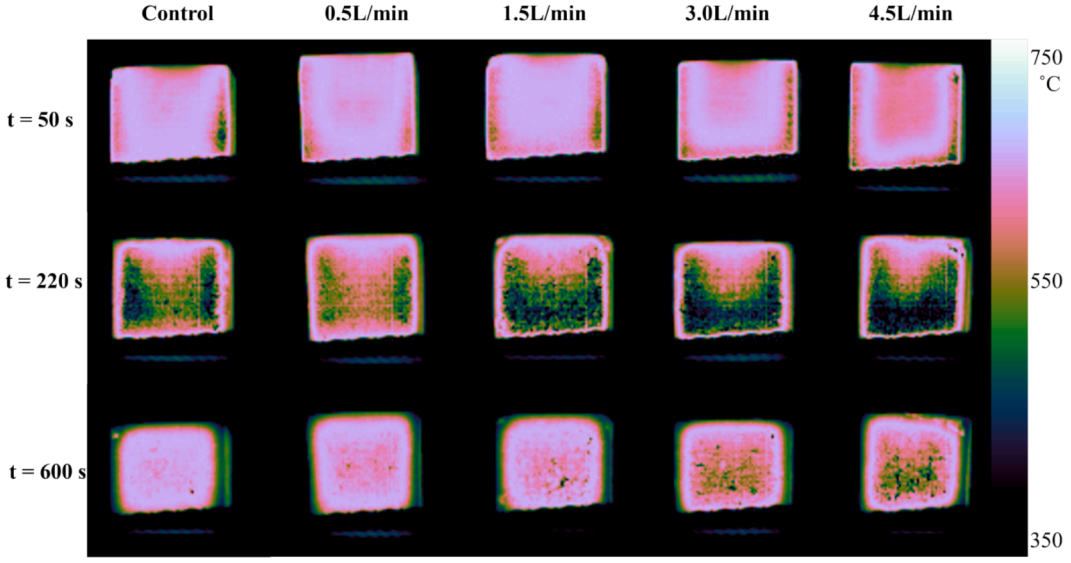

Fig. 4. Thermal images of charcoal sample at t = 50 s, 220 s and 600 s under different airflows.

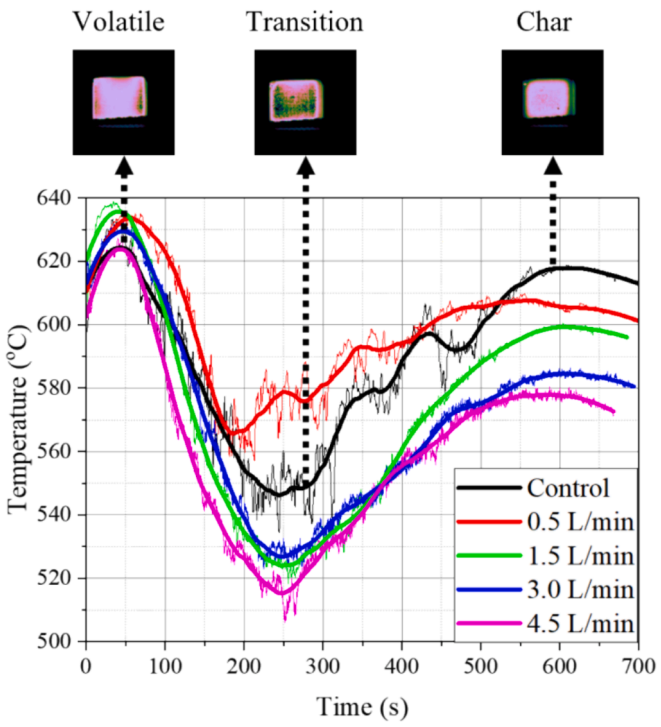

Fig. 5. Mean temperature of the side surface of the charcoal sample under different air flowrates. Thermal images show the typical stages of charcoal fuel under control air condition.

L/min) could facilitate the combustion process with increased oxygen availability. However, the cooling effects were more significant as the flowrate increased further, inhibiting the combustion process. Concurrently, the general temperature of the flow field above the burning charcoal was likely decreased because of the increased convective heat transfer rate [7]. Interestingly, the temperature profiles during the volatile combustion stage showed insiginificant variance across different airflow rates. However, as the combustion progressed from the volatile-dominant to the char-dominated phase, distinct temperature deviations emerged. This pattern suggests that the rate of airflow predominantly influences the char combustion stage, leading to temperature divergences. Char combustion, requiring higher temperatures for initiation compared to volatile matter [31] is governed by higher activation energies, as reported by the kinetic studies [32]. A lower flowrate (0.5 L/min) provide higher amount of oxygen that leads to more complete and efficient combustion of char, initials the transition to char combustion earlier and sustains higher temperature. In contract, while higher airflow rates increased oxygen supply, they did not substantially elevate oxygen concentration but instead significantly cooled the surface. Therefore, the transition to the char combustion was delayed and the intensity of the initiation and char combustion was reduced.

3.3. HSI and gas emission profiles

The thermal profiles highlight the interplay between the competing influences of enhanced oxygen supply and increased convective cooling on the system temperature. Section 2.3 describes the procedures for processing the HSI. The reconstructed HSI in Fig. 6 provide detailed spatial and temporal information on gas emissions during the combustion process, presenting the effects of airflow supply from an additional perspective. Three significant gaseous species: CH_4, CO, and CO_2, were identified at their characteristic peaks, with temporal images acquired at 1, 5, 10, 15, and 25 min after ignition. The HSI were coloured after a global normalisation to ensure the comparable display between different experimental conditions. The HSI of the control group were compared with 4.5 L/min airflow in order to observe the effects of airflow on the distribution of gases. These images offer a direct view into the gas-phase dynamics of biomass charcoal.

Generally, the spectral radiance of all three gas species declined over time, indicating the decreased intensity of combustion with the consumption in the fuel. However, the spatial distribution, intensity, and rate of decrease vary considerably among these species, representing the transition of the different combustion stages.

CH_4 displayed a concentrated distribution close to the charcoal sample, suggesting its rapid production and consumption during the initial, intense combustion of volatiles. Its spectral radiance, although relatively weak, decreased significantly, almost disappearing after the 5-minute mark. This observation is in agreement with the temperature trends shown in Fig. 5, which suggest a transition to char-dominated combustion occurring around 250 s. Additionally, both the spectral radiance intensity and the spatial distribution of CH_4 show insignificant difference when the 4.5 L/min air supply was applied. This phenomenon indicates the limited effects of additional airflow on the volatile stage of combustion, supporting the finding from the thermal results in Fig. 5.

CO, in contrast, showed a spatial distribution extending further from the sample than CH_4, reflecting a less immediate but more sustained emission during the combustion process. The spectral radiance, which was initially lower than that of CO_2 but higher than CH_4, decreased slowly over time. This observation could be attributed to the slow and stable combustion of char, in which CO is primarily produced [32]. The relatively consistent and high intensity of CO from 5-minute mark align with the observed combustion stage transition in Fig. 5.

CO_2 presented the highest intensity and the broadest spatial distribution among the three species, indicating its significant production

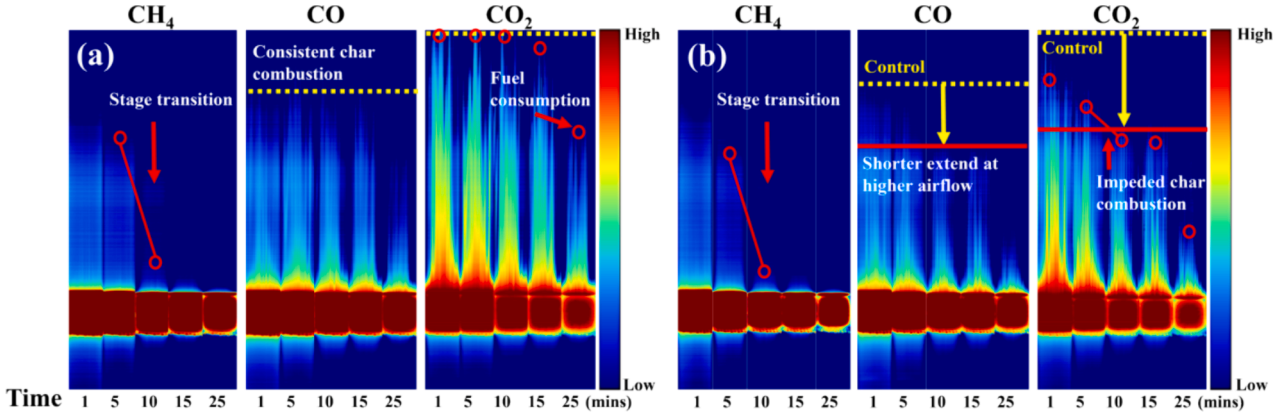

Fig. 6. Reconstructed HSI at typical peaks and under different time points showing the changes in intensity and distribution with time and varied airflow. (a) Control and (b) 4.5 L/min.

throughout the combustion process. Although it has the highest intensity, it also showed a steep, negative trend over time.

It is worth noting that the distribution regions and spectral radiance intensity of CO and CO_2 under 4.5 L/min airflow (Fig. 6(b)) exhibited reduced vertical extents than the control group (Fig. 6(a)). Given these two gases are the primary product of char combustion, this diminishment in both intensity and distribution could indicate a suppression of char combustion at high airflow rates. which has been demonstrated in Section 3.2. Saxena [28] introduced a two-region model for the CO and CO_2 concentration profile above a burning coal particle. This model explains the two specific regions of the oxidation of carbon. In the diffusion region (region I), the carbon in the coal reacts with the diffused oxygen and forms CO and CO_2, shown as Eqs. (6) and (7). In the reaction zone (region II), CO is consumed when it further reacts with the oxygen and forms CO_2, shown as Eq. (8).

$$C(s) + 1/2O_2(g) = CO(g) \tag{6}$$

$$C(s) + O_2(g) = CO_2(g) \tag{7}$$

$$CO(g) + 1/2O_2(g) = CO_2(g), \tag{8}$$

The dimension of these regions is a function of oxygen concentration. Our observations provided a direct view of the gas distributions under air supply. Fig. 6(b) shows a good agreement with the proposed model [28]. With increasing airflow rate, the radius of both region I (diffusion) and region II (reaction) decreased. This was due to the enhanced diffusion into the surface with the additional oxygen.

The spectral radiance values depicted in Fig. 6 qualitatively illustrate the spatial distribution and temporal evolution of each species while they do not enable a direct comparison in the combustion efficiency since the temperature dependent nature. Fig. 7 presents the relative percentage of the spectral radiance emitted by the gas-phase products, including H_2O, CH_4, CO_2, and CO emissions under different airflow rates. The percentage of gas species represents the status of combustion process (gas-phase combustion and solid-phase combustion balance) and the combustion efficiency. Generally, a larger percentage of CO_2 and H_2O vapour indicates higher completeness of combustion and combustion efficiency [33,34]. The higher concentration of combustible gases (CO and CH_4) indicates a lower oxidation level and results in a lower combustion efficiency.

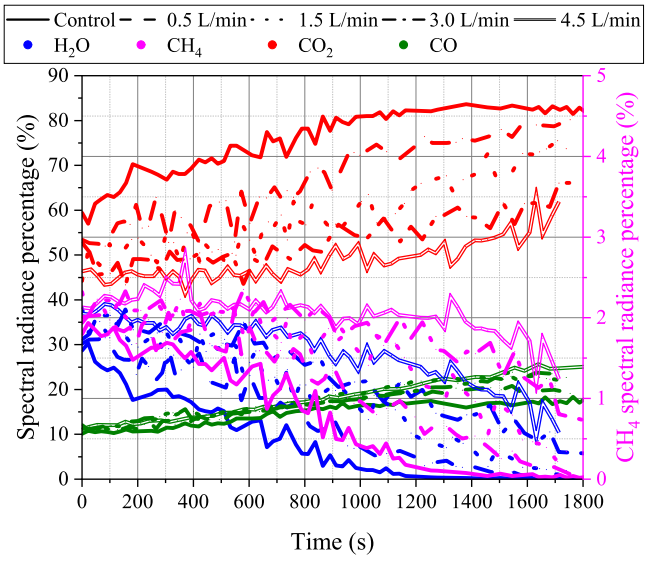

Fig. 7. The relative percentage of the spectral radiance emitted by the gas-phase products under different flow conditions: control – dash line; 0.5 L/min – dash line; 1.5 L/min – dot line; 3.0 L/min – dash dot; and 4.5 L/min – double line·H_2O, CO_2 and CO are presented with left y-axis. The CH_4 radiance is presented with right y-axis.

Among the species, CO_2 consistently dominated the emissions, which is given its role as the primary combustion product [33]. The percentage of CO_2 and CO emissions increased over time, in line with the progression of the combustion stages from volatile to char combustion [6]. Interestingly, the percentage of CO_2 decreased with higher airflow supply. This can be attributed to the lower forming rate to CO_2 explained by the Arrhenius Law, shown as Eq. (9) below:

$$k_r = A^*\exp(-\frac{E_a}{RT}) \tag{9}$$

where k is the reaction rate coefficient, T is the absolute temperature of the system, A is the pre-exponential factor, E_a is the activation energy for the reaction, and R is the universal gas constant.

In our analysis, we consider the convective and conductive heat transfer at the charcoal surface, assuming steady-state and one-dimensional conditions. The heat flux q is described by:

$$q = hS(T_s - T_{air}) + (-kS\frac{dT}{dx}) \tag{10}$$

where h is the convective heat transfer coefficient, T_s is the surface temperature, T_{air} is ambient temperature, k is thermal conductivity and S is the surface area. As the airflow rate increases, the velocity boundary layer at the charcoal surface reduces, leading to a thinner thermal boundary layer and a more pronounced temperature gradient, which enhances heat transfer through conduction. The increase in airflow also elevates the local Reynolds number (Re_x), enhancing the Nusselt number (Nu) —a function of both Reynolds and Prandtl numbers (Pr) under laminar and turbulent conditions over a flat plate. According to the definition $Nu = \frac{h}{k/L}$, this results in an increased convective heat transfer coefficient, thus amplifying heat loss through convection. These dynamics lead to a decrease in the system temperature, which in turn reduces the reaction rate coefficient according to Eq. (9).

The percentage of CO increased with higher airflow supply. This was attributed to two factors: On the one hand, the higher flowrate enhanced the diffusion of oxygen to the charcoal surface, facilitating the formation of CO (Eq. (5)). This has been demonstrated in Section 3.2 that the more effective diffusion with higher flowrate both in our observation and the reported model [28]. On the other hand, the decreased reaction rate k_r according to Eq. (9) reduced the consumption of CO in converting to CO_2, resulting in a higher percentage of CO.

The emissions of H_2O and CH_4 showed a decrease over time, peaking around 100 s, which aligned with their association with the initial volatile stage of biomass combustion [27] discussed in Section 3.2 with the surface temperature (Fig. 5). The CH_4 emission was more significance at higher airflow, suggesting a less combustion efficiency and a less intense of char combustion process, which typically requires a higher initiation temperature.

3.4. Emission ratios and combustion dynamics

In order to further investigate the effects of air flowrates on the combustion efficiency and dynamics, the ratios of spectral radiance of typical gases have been quantified and presented since the refers to the fraction of carbon released as CO_2 is an important indicator of the combustion completement [2,5]. Fig. 8 shows ratios of CO/CO_2, CH_4/CO_2 and H_2O/CO_2 emissions under varied airflow rates over time. These ratios provide crucial insights into the dynamics of combustion processes.

For CO/CO_2 ratio, an increasing trend was observed over time, and the ratio was found to be the highest at the maximum airflow rate (4.5 L/min). This trend evidences the discussion in Section 3.3 regarding the shift towards incomplete combustion with increased airflow rates, given that CO is a primary indicator of incomplete combustion [3]. This phenomenon was attributed to the enhanced diffusion from the solid

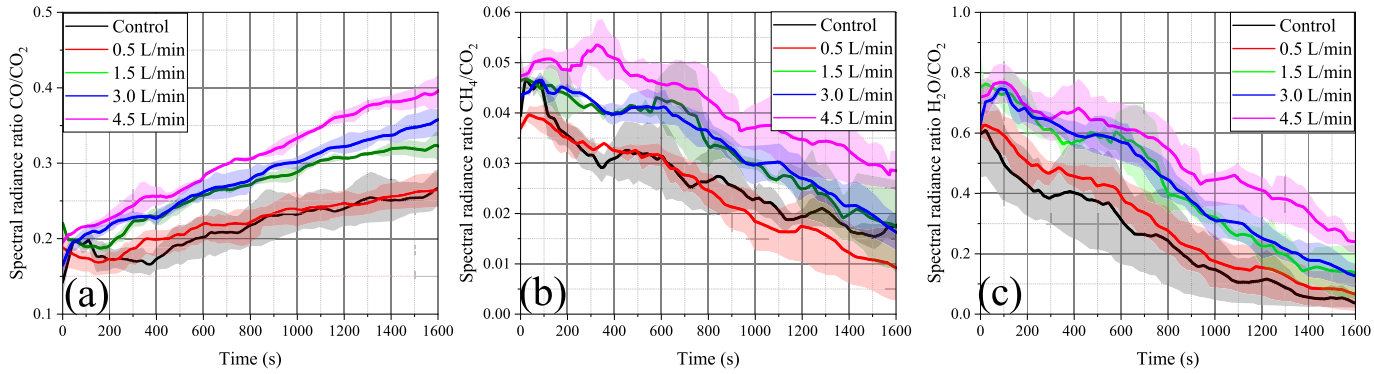

Fig. 8. The integrated spectral radiance ratio between gas products under various air flowrates. (a) CO/CO_2; (b) CH_4/CO_2; (c) H_2O/CO_2. Solid lines are the averaged values and shadows present the deviation.

fuel surface and decreased reaction rate caused by the significant cooling at higher flowrate, a higher level of CO would remain [28]. The quantitative results clearly illustrate while the overall combustion rate increased at high flowrate (as shown in Fig. 3), the efficiency of the combustion process correspondingly diminishes.

CH_4/CO_2 and H_2O/CO_2 ratios, which correlate to the volatile combustion stage, exhibited decreasing trends over time, with the lowest ratios observed at the control condition. Given the association of CH_4 and H_2O with the initial stages of biomass combustion, their decrease over time was consistent with the progressive consumption of these volatile compounds and aligned with the stage transition observed from the thermal profile (Fig. 5) and emission evolution (Fig. 6). Furthermore, higher CH_4/CO_2 ratio with the increased flowrate suggests a greater degree of incomplete combustion, as the efficiency of converting flammable gases to CO_2 diminishes. This reduced conversion efficiency is elucidated by Eq. (9), which associates lower system temperatures with higher airflow conditions. Conclusively, the increases observed in both CO/CO_2 and CH_4/CO_2 ratios under high airflow conditions signal a trend towards more incomplete combustion and reduced conversion efficiency, even though the overall rate of fuel consumption is increased.

Lastly, the H_2O/CO_2 ratio can represent the balance between gas-phase and solid-phase combustion·H_2O was predominantly produced during the gas-phase combustion, while CO_2 can be produced from both gas-phase and solid-phase combustion. Therefore, a lower H_2O/CO_2 ratio implies a progression towards enhanced solid-phase (char) combustion. This decrease over time suggests the gradual consumption of hydrogen within the charcoal fuel and a transition to the more stable char combustion phase, corroborating thermal and gas emission observations. The ratio reached its lowest at the control condition, indicating an increased predominance of solid-phase combustion at lower airflow rates. This trend is attributed to a more vigorous initiation of char reactions, facilitated by higher fuel temperatures associated with restricted airflow·H_2O/CO_2 ratio can also be considered as an indicator of the balance between pyrolysis and combustion are competing reactions within the charcoal combustion process. A higher H_2O/CO_2 ratio at higher flowrate directly reflects the shift in balance towards thermal pyrolysis. Such changes in thermal equilibrium towards pyrolysis rather than combustion could result from the decreased system temperature, as the lower trigger temperature of charcoal pyrolysis compared to self-sustained combustion. In addition, existed literature [28] reported that the oxygen in coal tends to be used up to form water with a low system temperature, while it tends to combine with carbon to produce oxides of carbon at higher temperature. This agreed well with our observations of the emission ratio and the surface temperature.

4. Conclusions

In this study, we provided a comprehensive characterisation of biomass charcoal combustion processes under varying forced airflow conditions using mid-wavelength infrared (MWIR) hyperspectral imaging (HSI) and long-wavelength infrared (LWIR) thermal imaging. The combined application of these advanced imaging techniques facilitated a multidimensional analysis of combustion dynamics, offering valuable insights into the spatial–temporal patterns of gas emissions, the transition from volatile to char combustion, combustion efficiency, the balance between the pyrolysis and combustion, as well as the implications of airflow variations on these processes. The charcoal sample was selected to represent the biofuels and the insights gained in this work could potentially help optimise the heterogeneous combustion system. The new visual-based technique proposed in this work holds new potentials in the biofuels research by providing both the flow and concentration fields of combustion products.

Key conclusions drawn from this study are as follows:

- Weight loss results indicated that the overall combustion rate accelerates with increased airflow, however, our multidimensional diagnostic approach, demonstrated that combustion efficiency concurrently decreases.
- The higher average surface temperature observed at the 0.5 L/min flow rate condition (up to 30 °C higher than the control and 65 °C higher than 4.5 L/min) revealed that lower airflow rates promote combustion process by balancing oxygen availability and cooling effects. Furthermore, significant temperature variations were observed after the transition from volatile to char stage (at ~250 s) suggested that higher airflow rates predominantly influence solid-phase combustion with reduced system temperature that is necessary for char reaction initiation.
- Hyperspectral imaging revealed distinct spatial distributions and temporal dynamics of key gas emissions (CH_4, CO, and CO_2) throughout the combustion process. It illustrated the combustion stage transitions and revealed the inhibition of char combustion by the high flow rates of air supply. The CO and CO_2 distributions were observed to be shortened with higher airflow rate, which was attributed to the enhanced diffusion.
- The observed spectral radiance ratios revealed shifts in combustion dynamics and lower efficiency with increased airflow. Notably, higher CO/CO_2 and CH_4/CO_2 ratios with increased airflow rates (approximately 60 % higher in CO/CO_2 and 67 % in CH_4/CO_2) were associated with reduced CO_2 formation, attributed to lower system temperatures and enhanced diffusion from the fuel surface. Additionally, increased H_2O/CO_2 ratios at higher airflow rates suggest a less intense char combustion and a shift towards pyrolysis over combustion, reflecting a decrease in the thermal equilibrium of the system.

CRediT authorship contribution statement

Yufeng Lai: Writing – review & editing, Writing – original draft,

Visualization, Validation, Software, Methodology, Investigation, Formal analysis, Data curation, Conceptualization. **Xuanqi Liu:** Writing – review & editing, Validation, Methodology, Investigation, Data curation, Conceptualization. **Muyi Pan:** Writing – review & editing, Validation, Software, Methodology, Investigation. **Matthew Davies:** Writing – review & editing, Software, Methodology, Investigation, Conceptualization. **Callum Fisk:** Writing – review & editing, Software, Methodology, Investigation. **David King:** Writing – review & editing, Software, Resources, Methodology. **Yang Zhang:** Writing – review & editing, Supervision, Resources. **Jon Willmott:** Writing – review & editing, Supervision, Software, Resources, Project administration, Investigation, Conceptualization.

Declaration of competing interest

The authors declare that they have no known competing financial interests or personal relationships that could have appeared to influence the work reported in this paper.

Data availability

Data will be made available on request.

References

[1] Wang B, Huang J, Wang Z, Xie D, Qiao Y. Interactions of potassium vapor with reactor tubes made of different materials and their impacts on particulate matter emission during pulverized biomass combustion. Proc Combust Inst 2023;39(3):3401–8. https://doi.org/10.1016/j.proci.2022.07.178.

[2] Cheng Z, Yang J, Zhou L, Liu Y, Wang Q. Characteristics of charcoal combustion and its effects on iron-ore sintering performance. Appl Energy 2016;161:364–74. https://doi.org/10.1016/j.apenergy.2015.09.095.

[3] Vicente ED, et al. Particulate and gaseous emissions from charcoal combustion in barbecue grills. Fuel Process Technol 2018;176:296–306. https://doi.org/10.1016/j.fuproc.2018.03.004.

[4] Lai Y, et al. Investigation of forced flow orientations on the burning behaviours of wooden rods using a synchronised multi-imaging system. Proc Combust Inst 2022. https://doi.org/10.1016/j.proci.2022.07.057.

[5] Jetter J, et al. Pollutant emissions and energy efficiency under controlled conditions for household biomass cookstoves and implications for metrics useful in setting international test standards. Environ Sci Technol 2012;46(19):10827–34. https://doi.org/10.1021/es301693f.

[6] Huang HL, Lee WMG, Wu FS. Emissions of air pollutants from indoor charcoal barbecue. J Hazard Mater 2016;302:198–207. https://doi.org/10.1016/j.jhazmat.2015.09.048.

[7] Evans DD, Emmons HW. Combustion of wood charcoal. Fire Saf J 1977;1(1):57–66. https://doi.org/10.1016/0379-7112(77)90008-X.

[8] Amato A, et al. Measurements and analysis of CO and O_2 emissions in $CH_4/CO_2/O_2$ flames. Proc Combust Inst 2011;33(2):3399–405. https://doi.org/10.1016/j.proci.2010.07.015.

[9] Akagi SK, et al. Emission factors for open and domestic biomass burning for use in atmospheric models. Atmos Chem Phys 2011;11(9):4039–72. https://doi.org/10.5194/acp-11-4039-2011.

[10] Yang H, et al. Experimental and simulated study of the relationship between color camera imaging and color-modeled equivalence ratio measurement. IEEE Trans Instrum Meas 2023;72. https://doi.org/10.1109/TIM.2023.3267359.

[11] Wang B, et al. Development of equivalence ratio measurement model of premixed methane flames using hyperspectral imaging of C2* and CH* chemiluminescence and random forest algorithm. Combust Sci Technol 2024. https://doi.org/10.1080/00102202.2024.2306899.

[12] A. S. Makowiecki *et al.*, "Mid-infrared dual frequency comb spectroscopy for combustion analysis from 2.8 to 5 μm," in *Proceedings of the Combustion Institute*, Elsevier Ltd, 2021, pp. 1627–1635. doi: 10.1016/j.proci.2020.06.195.

[13] Samimi-Abianeh O. Line-of-Sight optical diagnostic for measuring combustion products using species' natural emissions. Exp Therm Fluid Sci 2020;118. https://doi.org/10.1016/j.expthermflusci.2020.110174.

[14] Lai Y, et al. Combustion inhibition of biomass charcoal using slaked lime and dolime slurries. Fire Saf J 2023:103841. https://doi.org/10.1016/j.firesaf.2023.103841.

[15] F. L. Browne, "Theories of the combustion of wood and its control: a survey of the literature.".

[16] S. Bhattacharya, D. Albina, and P. Abdul Salam, "Emission factors of wood and charcoal-ÿred cookstoves," 2002.

[17] Liu X, Lai Y, Fisk C, Willmott J, Zhou H, Zhang Y. Experimental investigation on the effects of a mesh in the downstream region of a combustion-driven Rijke tube on self-excited thermoacoustic oscillations. Exp Therm Fluid Sci Jan. 2024;150. https://doi.org/10.1016/j.expthermflusci.2023.111061.

[18] Si M, Cheng Q, Zhang Q, Wang D, Luo Z, Lou C. Study of temperature, apparent spectral emissivity, and soot loading of a single burning coal particle using hyperspectral imaging technique. Combust Flame 2019;209:267–77. https://doi.org/10.1016/j.combustflame.2019.08.003.

[19] Lai Y, Wang X, Rockett TBO, Willmott JR, Zhang Y. Investigation into wind effects on fire spread on inclined wooden rods by multi-spectrum and schlieren imaging. Fire Saf J 2022;127. https://doi.org/10.1016/j.firesaf.2021.103513.

[20] Bertschi IT, Yokelson RJ, Ward DE, Christian TJ, Hao WM. Trace gas emissions from the production and use of domestic biofuels in Zambia measured by open-path Fourier transform infrared spectroscopy. J Geophys Res Atmos 2003;108(13). https://doi.org/10.1029/2002jd002158.

[21] Rothman LS, et al. The HITRAN2012 molecular spectroscopic database. J Quant Spectrosc Radiat Transf 2013;130:4–50. https://doi.org/10.1016/j.jqsrt.2013.07.002.

[22] J. Thé Riault, E. Puckrin, and H. Lavoie, "Remote Monitoring of Multi-gas Mixtures by Passive Standoff Fourier Transform Infrared Radiometry.".

[23] Lai Y, et al. Characterisation of wood combustion and emission under varying moisture contents using multiple imaging techniques. Fuel 2024;373:132397. https://doi.org/10.1016/j.fuel.2024.132397.

[24] Li K, Yan W, Huang X, Yu L, Chen Y, Lou C. In-situ measurement of temperature and potassium concentration during the combustion of biomass pellets based on the emission spectrum. Fuel 2021;289. https://doi.org/10.1016/j.fuel.2020.119863.

[25] Johansson R, Leckner B, Andersson K, Johnsson F. Account for variations in the H_2O to CO_2 molar ratio when modelling gaseous radiative heat transfer with the weighted-sum-of-grey-gases model. Combust Flame 2011;158(5):893–901. https://doi.org/10.1016/j.combustflame.2011.02.001.

[26] Glushkov DO, Nyashina GS, Anand R, Strizhak PA. Composition of gas produced from the direct combustion and pyrolysis of biomass. Process Saf Environ Prot 2021;156:43–56. https://doi.org/10.1016/j.psep.2021.09.039.

[27] Fang MX, Shen DK, Li YX, Yu CJ, Luo ZY, Cen KF. Kinetic study on pyrolysis and combustion of wood under different oxygen concentrations by using TG-FTIR analysis. J Anal Appl Pyrolysis 2006;77(1):22–7. https://doi.org/10.1016/j.jaap.2005.12.010.

[28] S. C. Saxena, "Devolatilization and combustion characteristics of coal particles," 1990.

[29] Abbassi MA, Grioui N, Halouani K, Zoulalian A, Zeghmati B. A practical approach for modelling and control of biomass pyrolysis pilot plant with heat recovery from combustion of pyrolysis products. Fuel Process Technol 2009;90(10):1278–85. https://doi.org/10.1016/j.fuproc.2009.06.010.

[30] Shan F, et al. An experimental study of ignition and combustion of single biomass pellets in air and oxy-fuel. Fuel 2017;188:277–84. https://doi.org/10.1016/j.fuel.2016.09.069.

[31] Kastanaki E, Vamvuka D. A comparative reactivity and kinetic study on the combustion of coal-biomass char blends. Fuel 2006;85(9):1186–93. https://doi.org/10.1016/j.fuel.2005.11.004.

[32] Morin M, Pécate S, Hémati M. Kinetic study of biomass char combustion in a low temperature fluidized bed reactor. Chem Eng J 2018;331:265–77. https://doi.org/10.1016/j.cej.2017.08.063.

[33] Jimenez J, Farias O, Quiroz R, Yañez J. Emission factors of particulate matter, polycyclic aromatic hydrocarbons, and levoglucosan from wood combustion in south-central Chile. J Air Waste Manage Assoc 2017;67(7):806–13. https://doi.org/10.1080/10962247.2017.1295114.

[34] R. Koppmann, K. Von Czapiewski, and J. S. Reid, "A review of biomass burning emissions, part I," 2005. [Online]. Available: www.atmos-chem-phys.org/acpd/5/10455/SRef-ID:1680-7375/acpd/2005-5-10455EuropeanGeosciencesUnion.